Characterization of cryogenic sloshing via image velocimetry, free surface tracking and data assimilation

Pedro Afonso Marques[1,2,*], Alessia Simonini[1], Mathieu Delsipée[1], Miguel Alfonso Mendez[1]

1: Environmental and Applied Fluid Dynamics, von Karman Institute for Fluid Dynamics, Waterloosesteenweg 72, Sint-Genesius-Rode, 1640 , Belgium Brussels, 1050, Belgium
2: Transferts, Interfaces Et Procédés (TIPs), Université Libre de Bruxelles, Av. Franklin Roosevelt 50

*Corresponding author: pedro.marques@vki.ac.be

Keywords: RBF, meshless algorithm, PTV, cryogenic, multiphase flow, sloshing.

ABSTRACT

Cryogenic fuels such as liquid hydrogen (LH_2) and liquified natural gas (LNG) are promising energy carriers for the future. Their thermal management is significantly challenged by the liquid sloshing induced by external acceleration because sloshing strongly impacts the evaporation rate and, thus, the reservoir's pressure control. This work presents a unique experimental characterization of liquid sloshing in cryogenic conditions combining interface tracking, image velocimetry and physics-constrained data assimilation. The experiments were conducted in a reduced-scale cryogenic tank partly filled with liquid nitrogen undergoing lateral harmonic sloshing. A combination of floating and neutrally buoyant seeding particles was used to simultaneously carry out interface tracking using a moving-window Radon transform and image velocimetry using Particle Tracking Velocimetry (PTV). The data assimilation was carried out using constrained radial basis function (RBF) regression, imposing kinematic boundary conditions at the walls and interface. The assimilation allows for unprecedented super-resolution of the velocity field.

1. Introduction

The ongoing energy crisis has driven several industries toward sustainable energy solutions. Cryogenic propellants such as liquid hydrogen (LH_2) and liquefied natural gas (LNG) have emerged as highly promising green options. These fuels can have low pollutant emissions (Ball & Wietschel, 2001) and high specific energy (Fortescue et al., 2003) but must be stored at extremely low temperatures (-250 °C for LH_2 and -170 °C for LNG). Continuous developments in cryogenic technologies are making these temperatures more and more accessible, thus making cryogenic fuels attractive also in sectors such as aeronautics (Verstraete et al., 2010) and shipping (Jeon et al., 2021).

Nevertheless, the thermal management of cryogenic fuel storage in vehicles such as airplanes or vessels is particularly challenging because of propellant sloshing. Besides challenging stability and maneuverability, sloshing enhances thermal mixing and mass transfer between ullage gas

and liquid propellant. This causes strong pressure oscillation that could compromise the tank's structural stability and hinder the smooth supply of fuel to the engine. While these aspects have been the focus of many investigations for spacecrafts (Abramson et al., 1966; Moran et al., 1994; Barsi, 2010; Ludwig et al., 2013; Moya et al., 2019; Bäuerlein & Avila, 2021), further work is required to minimize the harmful impact of sloshing and thereby extend cryogenic propulsive technologies beyond the aerospace industry.

While the literature on the sloshing dynamics is abundant, bolstered during the 1950s and 1960s by the space race (Abramson et al., 1966), most cryogenic experiments are carried out intrusively (e.g., with load cells, strain gauges, level-sensing probes) and without visualization due to the harsh insulation requirements. Recently, some authors have employed imaging techniques to characterize sloshing flows. In particular, Simonini et al. (2016) and Davin et al. (2023) employed velocimetry techniques such as PIV (Particle Image Velocimetry) and PTV (Particle Tracking Velocimetry) to retrieve velocity fields in the entire liquid domain. However, as reported in Simonini et al. (2016), Simonini, Peveroni, & Vetrano (2019) and Fonda et al. (2012), image velocimetry in cryogenic conditions remains particularly challenging both in terms of experimental setup and data processing. On the setup side, the first difficulty is in the identification and the introduction of seeding particles in a cryogenic test section. Besides the lack of commercial solutions for particles matching the density of most cryogenic liquids and the strong dependency of the liquid's density on temperature, the seeding procedure must remove moisture to avoid ice formation and particle agglomeration. Moreover, the illumination must be carried out with a low-intensity laser to avoid overheating the liquid and producing buoyancy-driven flows. On the processing side, the presence of the moving free interface challenges the image interrogation (Simonini et al., 2016). Correlation-based approaches must deal with the large deformation of the domain due to the interface motion. The PIV Adaptive Interrogation and Sampling with Image Projection (PAISSIIP) algorithm by Simonini, Theunissen, et al. (2019) can handle the interface deformation but cannot overcome the limitations in spatial modulation implied by any cross-correlation-based approach. On the other hand, tracking-based methods suffer from a lack of particles near the interface and the difficulty of distinguishing the motion of seeding particles from the motion of the interface.

Building on the expertise developed in Simonini et al. (2016), we focus on the processing challenges. We propose a novel methodology to augment the resolution of tracking velocimetry near a moving interface by combining (1) interface tracking, (2) PTV, and (3) data assimilation via constrained RBF regression (Sperotto et al., 2022). We detect the interface by seeding the flow with low-density particles that float on the surface. The detection algorithm is based on a windowing approach relying on the Radon transform to identify the lines along which the floating particles are located (Simonini, Peveroni, & Vetrano, 2019). On the other hand, for PTV, we seed the flow with particles whose density closely matches the liquid. We process the acquired images through the open-source TracTrac software (Heyman, 2019), generating a two-dimensional unstructured grid for the liquid's velocity field during sloshing. Lastly, the data assimilation is carried out using the open-source software SPICY (Super-resolution and Pressure from Image veloCimetrY) (Sperotto et al., 2024). This software performs data assimilation from image velocimetry data using the

constrained RBF regression framework originally proposed in Sperotto et al. (2022). This allows to impose physics-based constraints (e.g., divergence-free flow, Dirichlet, and Neumann boundary conditions) and for computing the associated pressure distribution. We use the constraint formalism to enforce the interface kinematics on the velocity field regression.

Our methodology is applied on cryogenic experimental data acquired in the von Karman Institute. The experimental campaign is carried out in the CryME (Cryogenic Microgravity Experiments) cryostat, which is capable of holding reduced-scale models of propellant tanks filled with liquid nitrogen (LN_2). We consider lateral harmonic excitation to produce lateral planar sloshing.

The rest of this article is structured as follows. Section 2 presents the experimental set up and the testing conditions. Section 3 reports on the data processing, including interface tracking, PTV and data assimilation. Section 4 collects the preliminary results while section 5 closes with conclusions and outlook.

2. Experimental methods

This section describes the experimental set up in 2.1 and the testing conditions in 2.2

2.1. Experimental setup

The experimental setup, shown in Figure 1, comprises five major components: (1) a reduced-scale tank partly filled with LN_2, (2) a bath cryostat to maintain the test cell at cryogenic temperatures, (3) a shaking table to induce sloshing, (4) optics to shape the laser into a sheet, and (5) the acquisition system. The reduced-scale tank is made of quartz, allowing for optical access. It consists of a rectangular cuboid with outer dimensions of 100 mm by 100 mm and 134 mm in height, drilled with a circular hole with a diameter of 80 mm and a depth of 124 mm. The outer cuboid shape is designed to minimize image distortions due to the inner curved surface as discussed in Simonini, Peveroni, & Vetrano (2019).

The reduced-scale tank is installed in the cryostat. This comprises four essential components: the LN2 reservoir, a sample space, an heat exchanger and a vacuum chamber. The reservoir chills down the sample space through the heat exchanger. The temperature in the sample space is precisely controlled in the range 75-85 K a regulator. The sample space is initially filled with gaseous helium at 0.3 bara, maximizing its thermal conductivity and temperature uniformity. Once the desired working temperature is reached, the helium is removed from the volume and kept under vacuum. Lastly, the vacuum chamber separates the outer environment from the inner volumes of the cryostat. The vacuum minimizes heat exchanges from the surroundings to the inside of the setup and allows to set stable thermal conditions throughout the measurements.

The cryostat holding the quartz tank is mounted on the von Karman Institute's SHAKESPEARE (SHaking Apparatus for Kinetic Experiments of Sloshing Projects with EArthquake Reproduction)

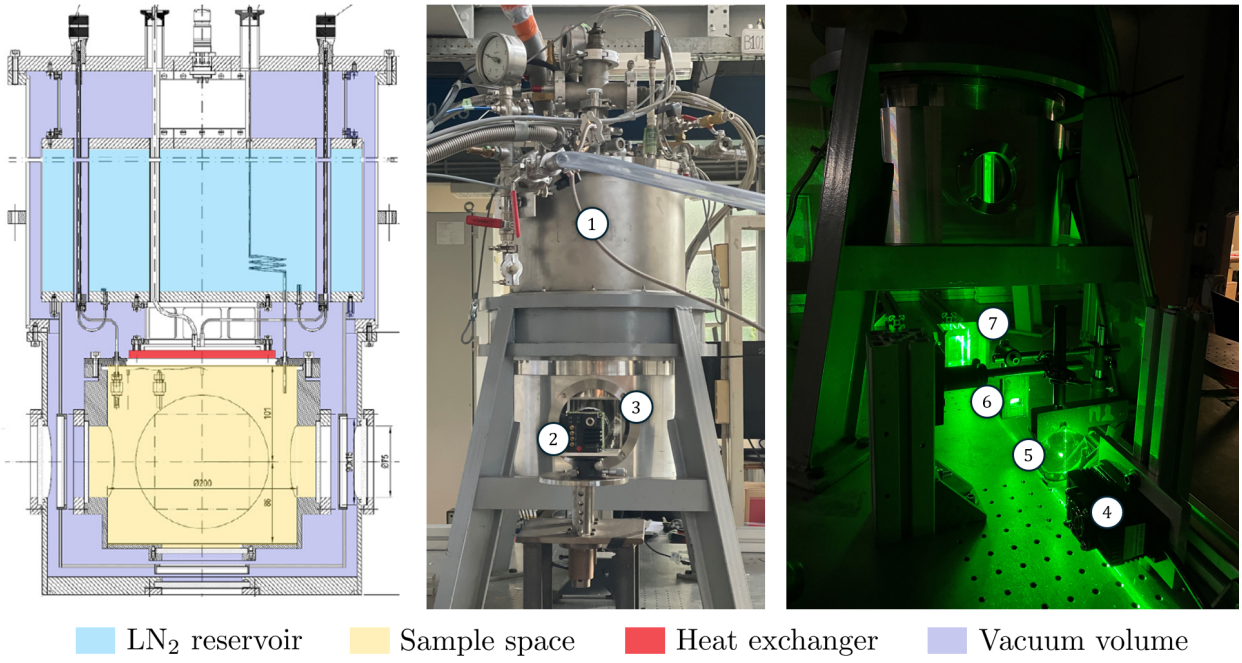

Figure 1. Overview of the experimental setup. The figures on the left and center showcase a schematic and photo, respectively, of the CryME cryostat, while the optical setup is on the right. The numbering identifies: (1) bath cryostat, (2) camera, (3) viewport to the reduced-scale tank, (4) laser head, (5) spherical lens, (6) cylindrical lens, (7) prism.

facility. This facility has three sliding modules that reproduce three-dimensional accelerations with controlled amplitudes and frequencies. The resulting forcing excitations are recorded via a triaxial Endevco Model 7298 accelerometer and an ODS-30 optical displacement sensor. The temperature conditions in the tank are monitored through an array of Lakeshore DT-670-SD thermo-diodes, while a fast-response Kulite CTL-190 measures the pressure. Given the optical access provided by the cryostat and the quartz tank, we acquire flow images using a JAI SP-1200M-CXP4 camera at 75 Hz. The illumination is provided by a DPSSL Driver II continuous laser (wavelength 532 nm, power 0.8W), focused and shaped into a sheet as illustrated in Figure 1 on the right, i.e. passing underneath the cryostat's bottom window and illuminating its mid-plane. The fluid is seeded with both neutrally buoyant and floating hollow glass spheres. The firsts have a diameter in the range $5 - 15$ μm and match the LN_2 density of 830 kg/m^3 at 72 K. The density miss-match is at most at 2% at 76 K. The floating particles have a diameter in the range $5 - 20$ μm and a density of 790 kg/m^3. Given enough settling time, these particles float toward the free surface, allowing for the interface detection algorithm described in Section 3.1. We introduce the seeding in the tank before mounting it inside the cryostat. We purge the tank several times with gas nitrogen to minimize moisture between the particles, which creates agglomerations (Simonini et al., 2016).

2.2. Testing conditions

Once the cryostat is purged and chilled down to 77 K, we proceed with the filling of LN2. This quickly vaporizes until the reservoir reaches 1 bara (the saturation pressure at 77 K). From that

condition, further injections of LN2 remain in saturated liquid conditions and fill the tank. The fill level is adjusted by visual inspection with the help of a millimetric grid attached to the lateral edge of the quartz. We fill the tank to a depth of 60 mm.

In this work we consider sloshing produced by lateral harmonic oscillations in the vicinity of the natural frequency corresponding to the first asymmetrical mode (Ibrahim, 2005)

$$\omega_{11} = \left(\frac{g\xi_{mn}}{R} + \frac{\sigma}{\rho_l} \frac{\xi_{mn}^3}{R^3} \right) \tanh \left(\frac{\xi_{mn} H_l}{R} \right) \tag{1}$$

where $m = n = 1$ are the indices defining the order of the sloshing mode, ξ_{mn} is the nth zero of the first derivative of the m$^{\text{th}}$ order Bessel function, σ is the surface tension, ρ_l is the liquid density, H_l is the fill level, and R is the tank radius. According to Miles' weakly nonlinear theory (Miles, 1984), exciting upright cylinders near ω_{11} triggers three major wave responses: planar waves, chaotic sloshing, and swirl waves (see also Marques et al. (2023)). We here focus on the first, which produces a 2D dynamics in the mid-plane, where our planar measurements are conducted. This regime is characterized by a nearly flat interface, harmonically oscillating at the excitation frequency. This condition can be well described by linear analytical models, that will be used to validate the measurements in the full version of this article.

3. Data Processing

This section describes the data processing techniques for the interface detection, image velocimetry with PTV, and physics-constrained RBF regression. All images acquired during the experiments are filtered to reduce noise, and their background is removed through a POD-based (Proper Orthogonal Decomposition) approach by Mendez et al. (2017). Moreover, we adjust the image brightness through a γ correction and apply a high-pass spatial filter to highlight the seeding in the images.

3.1. Free surface detection

The laser illumination makes the floating particles clearly visible. Since these float at a close distance, the interface appears as a collection of piece-wise continuous lines. Our algorithm, following Simonini, Peveroni, & Vetrano (2019), relies on the Radon transform. This integrates the image's pixel intensities along lines offset by r from the center of the image, inclined by an angle θ. This transform maps the image's Cartesian (x, y) frame to a polar coordinate system (r, θ) with its origin on the image centroid. By identifying the brightest point on the transformed image, we retrieve the line on the original image with the most illuminated pixels.

Since the acquired images display many particles, most of which belong to the bulk liquid and to mirror reflections above the interface, we employ a variation of the multi-step procedure proposed

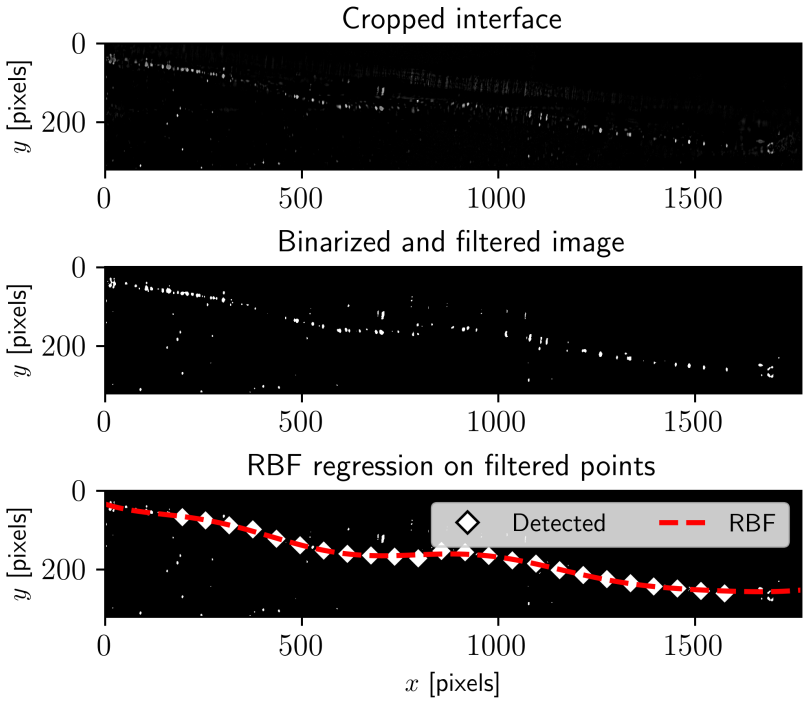

Figure 2. Different stages of the Radon transform interface detection algorithm. Upper: pre-procesed images cropped around the interface. Center: binarized and filtered image. Lower: detection points in each window centroid (diamond marks) and RBF regression (dashed line).

in Simonini, Peveroni, & Vetrano (2019). First, the full image is cropped, restricting the region of interest (ROI) to the free surface, thereby minimizing the number of outlier particles in the detection. Then, the images are binarized following Otsu's method (Otsu, 1979). Subsequently, we divide the image in several windows along the spanwise direction of the interface, with a user-defined width and overlap. By applying the Radon transform to each window, we extract the direction with the highest intensity pixels and, therefore, the straight line most closely aligned with the particles floating on the interface. We take the middle point of each line as the detected interface position in each window. Once all points are retrieved, the outliers are filtered out through a moving median filter. The remaining points are fitted to RBFs with pre-defined collocation points and shape factors. Thus, we extract a smooth analytical expression for $\eta(x,t)$. Figure 2 displays the main steps in the algorithm.

3.2. Particle Tracking Velocimetry

This work employs the TracTrac open-source code, described in Heyman (2019), for the PTV analysis. The algorithm consists of three main stages: (1) object detection, (2) motion estimation, and (3) error monitoring. We mask the acquired images above the free surface to minimize detecting reflections and optical aberrations at the interface. Hence, the algorithm is only applied to detect the motion of particles in the liquid. The particles are detected based on a user-defined intensity

threshold and pairing between frames. The detected particles are then compared with their nearest neighbours along subsequent frames. Since some particles appear and disappear between images, a forward and backward computation is carried out, and only unequivocal pairs are preserved. Moreover, TracTrac uses the previous frame's velocity field as a predictor for the subsequent one, setting up an iterative process where the predicted and detected velocities are compared to identify outliers. Consequently, we obtain a smoothed velocity field where spurious velocities are replaced by interpolating the neighbouring velocities.

3.3. Physics-constrained velocimetry

The velocity fields obtained by PTV are then loaded into the SPICY software (Sperotto et al., 2024). This software allows to provide an analytic (differentiable) approximation of the velocity field that respects boundary conditions and differential constraints such as divergence free conditions. The velocity field at each time step is approximated by a linear combination of RBFs:

$$\boldsymbol{u}(\boldsymbol{x}, t_k) \approx \tilde{\boldsymbol{u}}(\boldsymbol{x}, t_k) = \sum_{k=1}^{n_b} w_k(t_k)\varphi_k(\boldsymbol{x}|\boldsymbol{x}_k^*, \boldsymbol{c}_k) \tag{2}$$

where w_k represents the weights to be identified from the velocimetry data, φ_k spans the n_b basis elements, $\boldsymbol{x} = (x, y)$ is the set of points over which predictions are requested, $\boldsymbol{x}_k^*$ is the vector of RBFs collocation points and $\boldsymbol{c}_k$ is the vector of shape factors associated with each basis element. The reader is referred to Sperotto et al. (2022) for more details on the mathematical background. SPICY employs the K-means clustering algorithm (Sculley, 2010) to define the collocation points $\boldsymbol{x}_k^*$ and shape factors $\boldsymbol{c}_k$, aiming to distribute an equal number of particles per RBF.

The RBF regression consists in identifying the weights $w_k(t_k)$ in (2) such that (1) the regression agrees with the velocity data available at the particle location and (2) certain constraints are satisfied. This is achieved by identifying the optimal sets of weights $\boldsymbol{w}$ that minimize the augmented cost function $\mathcal{A}(\boldsymbol{w})$, defined as

$$\mathcal{A}(\boldsymbol{w}) = ||\boldsymbol{u}(\boldsymbol{x}) - \boldsymbol{\Phi}(\boldsymbol{X})\boldsymbol{w}||_2^2 + \boldsymbol{\alpha}\boldsymbol{P}(\boldsymbol{w}) + \boldsymbol{\lambda}^T\boldsymbol{H}(\boldsymbol{w}) \tag{3}$$

where $\boldsymbol{\Phi}(\boldsymbol{X}) \in \mathbb{R}^{n_p \times n_b}$ is the matrix containing all basis functions defined in the domain $\boldsymbol{X} \in \mathbb{R}^{n_p}$, $\boldsymbol{\alpha}$ is the vector of user-defined penalty factors, $\boldsymbol{P}(\boldsymbol{w})$ encompasses all *quadratic* penalties, $\boldsymbol{\lambda}$ is the vector of Lagrange multipliers associated with the *linear* constraints $\boldsymbol{H}(\boldsymbol{w})$. Regarding penalties, since (3) is typically an ill-posed problem (Bishop, 2006), SPICY employs a Tikhonov regularization to stabilize the numerical methods underlying the optimization (Sperotto et al., 2022).

Figure 3 summarizes the penalties and constraints applied in the current work. In addition to the Tikhonov regularization, we employ the divergence-free condition as a global penalty $||\nabla \cdot \boldsymbol{\Phi}(\boldsymbol{X}) = 0||_2$. Furthermore, we impose that the lower surface of the bulk and the lateral edges $\boldsymbol{X}_D \in \mathbb{R}^{2n_D}$ have a zero velocity (Dirichlet constraint) $\boldsymbol{\Phi}(\boldsymbol{X}_D) = 0$.

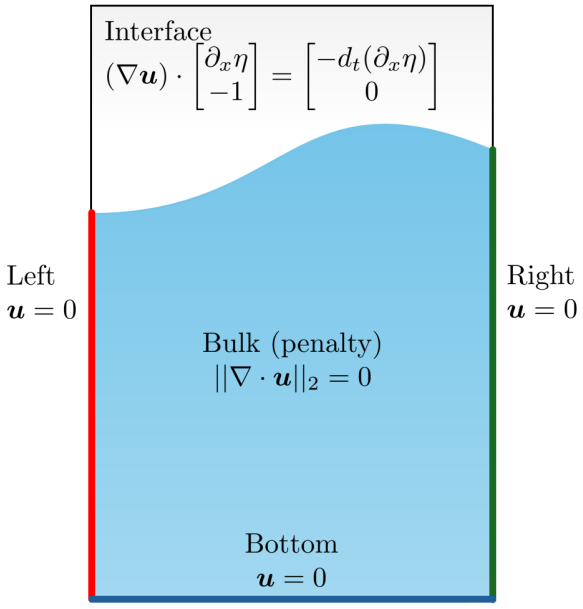

Figure 3. Schematic of the flow boundary conditions on the left, right, bottom and interface edges applied as constraints. The divergence-free condition is applied as a penalty in the bulk.

Lastly, and perhaps most interestingly to the problem at hand, we introduce the kinematic condition on the interface points $\boldsymbol{X}_\eta \in \mathbb{R}^{2n_\eta}$ as a additional constraint. Considering a two-dimensional slice of the domain, the interface position η is expressed solely as function of the horizontal coordinate (x) and time (t). Denoting as $\boldsymbol{u}|_h(x,y,t) = [u|_h, v|_h]^T$ the velocity vector at an interface location, the kinematic condition ensuring the continuity of the free surface $\eta(x,t)$ (Ibrahim, 2005) is

$$v|_h = \frac{\partial \eta}{\partial x} u|_h + \frac{d\eta}{dt}. \tag{4}$$

To impose the interface's kinematics in SPICY, we transform (4) into a Neumann condition. This is achieved by first differentiating (4) with respect to x and y, and then neglecting "small terms" under the assumption of gently sloped interface. One thus has:

$$\begin{cases} \left.\dfrac{\partial v}{\partial x}\right|_h = \dfrac{\partial^2 \eta}{\partial x^2} u|_h + \left.\dfrac{\partial \eta}{\partial x}\dfrac{\partial u}{\partial x}\right|_h + \dfrac{\partial}{\partial x}\left(\dfrac{d\eta}{dt}\right) \approx \left.\dfrac{\partial \eta}{\partial x}\dfrac{\partial u}{\partial x}\right|_h + \dfrac{d}{dt}\left(\dfrac{\partial \eta}{\partial x}\right) \\ \left.\dfrac{\partial v}{\partial y}\right|_h = \dfrac{\partial}{\partial y}\left(\dfrac{\partial \eta}{\partial x}\right) + \left.\dfrac{\partial \eta}{\partial x}\dfrac{\partial u}{\partial y}\right|_h + \dfrac{\partial}{\partial y}\left(\dfrac{d\eta}{dt}\right) = \left.\dfrac{\partial \eta}{\partial x}\dfrac{\partial u}{\partial y}\right|_h \end{cases} \tag{5}$$

Therefore, (5) can be shaped into a Neumann boundary condition of the form

$$\begin{bmatrix} \partial_x u & \partial_x v \\ \partial_y u & \partial_y v \end{bmatrix} \begin{bmatrix} \partial_x \eta \\ -1 \end{bmatrix} = \begin{bmatrix} -d_t(\partial_x \eta) \\ 0 \end{bmatrix}, \tag{6}$$

compatible with the general SPICY's template for Neumann conditions $(\nabla \boldsymbol{\Phi}(\boldsymbol{X}_\eta)) \cdot \boldsymbol{n}_\eta = \boldsymbol{c}_\eta$, where $\boldsymbol{n}_\eta = [\partial_x \eta, -1]^T$ and $\boldsymbol{c}_\eta = [-d_t(\partial_x \eta), 0]^T$ and d_t denoting time differentiation. From the interface

detection described in Section 3.1 we first compute $\partial_x \eta$ analytically, since this is also approximated via RBF regression. Then, we compute its rate-of-change $d_t(\partial_x \eta)$ by finite differences on consecutive frames and impose (6) to the regression of velocity fields.

4. Results and discussion

This section presents preliminary results of the interface dynamics and velocity fields during sloshing.

Figure 4 shows a representative snapshot of the velocity field during planar sloshing, where the detected interface position is plotted in white. The applied constraints and penalties correspond to 'Case 3' in Table 1.

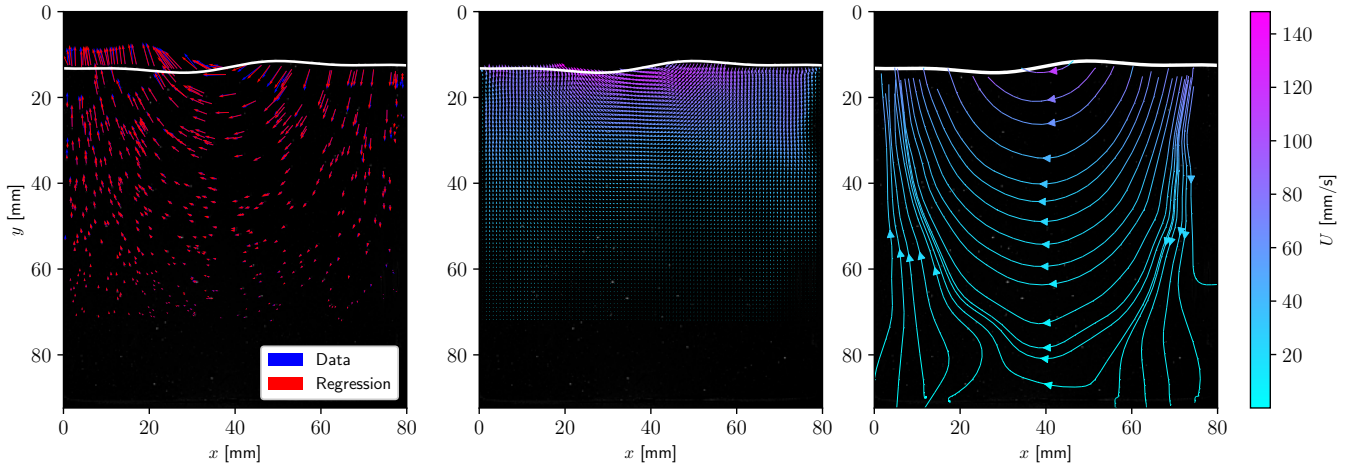

Figure 4. Comparison of the PTV data with the RBF regression for one snapshot. Left: velocity field retrieved from TracTrac (blue) compared against the SPICY results (red). Center: physics-constrained velocity field evaluated on a 100×100 grid. Right: Streamlines computed on the same grid.

The leftmost quiver plot compares the velocimetry data extracted from TracTrac with the regressed velocity field. An excellent agreement in the measurement points is observed, especially in the central region of the bulk. The global relative l_2 error for the regression is of the order of 10.2 % in the u component and 9.4 % in v. These values are particularly encouraging if one considers that the l_2 norm of the measurements is particularly low since the velocity is near zero in a large portion of the measurement domain. The largest discrepancies happen near the interface, where larger gradients can be expected.

This mismatch is partly explained by the larger signal-to-noise ratio near the free surface, which might hamper the particle detection and motion prediction in the PTV algorithm. Moreover, we rely on accurately tracking the interface to impose the proper dynamic boundary conditions during the regression. Thus, since this corresponds to a high uncertainty region for the PTV and regressed data, it is expected that the largest discrepancies would be detected here.

The central plot presents the regressed velocity on a uniform 100×100 grid. By imposing the interface's dynamic conditions as a physical constraint to the regression, we ensure that the flow drives the interface motion. Thus, we obtain a fully consistent velocity field from which we can characterize the sloshing dynamics. From the rightmost plot, we show the streamlines corresponding to the regressed velocity field. The figure shows the expected vortex-like flow (Ibrahim, 2005), which mixes the liquid in the upper regions of the interface towards the bulk and vice-versa.

Table 1. Parameters of the velocity regression using SCIPY for the same velocity snapshot shown in Figure 4. Three cases were evaluated using different constraints, keeping the same divergence-free penalty with a magnitude $\alpha = 100$. The Dirichlet and interface dynamics constraints are employed on n_D and n_η points, respectively.

Case	$\nabla \cdot \boldsymbol{u} = 0$	n_D	n_η	$\|\|u - \tilde{u}\|\|_2^2[\%]$	$\|\|v - \tilde{v}\|\|_2^2[\%]$
1	$\alpha = 100$	0	0	12.1	7.6
2	$\alpha = 100$	598	0	12.6	9.9
3	$\alpha = 100$	598	200	10.2	9.4

Table 1 shows the regression errors on the same snapshot as Figure 4. We considered three test cases, keeping the divergence-free condition with a penalty term of 100. The first case employs no constraints, while the second only accounts for the zero velocity at the solid boundaries. Lastly, the third case enforces the interface's dynamic conditions. Remarkably, the interface's kinematic constraint ('Case 3'), the regression error in the u component improves by 1.9% relative to 'Case 1' and 2.4 % relative to 'Case 2'. On the other hand, the error in the v component increases when constraints are added. This is likely tied to differences in computing the velocity of the fluid near the lateral edges, which lack seeding, thus modifying the shape of the streamlines in the bulk. Nevertheless, our results show that constraining the regression with the interface dynamics can improve the regression while providing a fully consistent velocity field with respect to the interface motion.

5. Conclusions and outlook

This work presents a novel methodology for experimentally characterizing sloshing flows. We combine bulk velocity data from image velocimetry with interface dynamics extracted from a Radon transform-based interface tracking algorithm. The experiments were carried out in an upright cylindrical tank partly filled with liquid nitrogen, undergoing lateral sloshing. The liquid was seeded with hollow glass spheres, allowing simultaneous interface tracking and bulk velocity measurements.

The interface tracking algorithm allowed for accurately detecting the displacement of the free surface during sloshing. The detected points were then regressed via a linear combination of RBFs to smooth out small detection irregularities and allow for the full interface position to be known. In future investigations, this regression will be constrained to impose physical conditions such as contact line dynamics.

The velocity field in the bulk liquid was measured through PTV. Here, we used the detected interface position at each frame to mask out the parts of the image not belonging to the liquid phase. Thus, we minimized the errors due to the erroneous detection of reflections and lighting artifacts. While the PTV algorithm successfully detected particle motion in most of the liquid, it struggled due to a lack of seeding near the walls, especially toward the deepest portions of the bulk. The challenges with the seeding are partly attributed to the entrainment of humidity between the particles, leading to their agglomeration (Simonini, Peveroni, & Vetrano, 2019). Nevertheless, we retrieved the 'vortex-like' flow pattern characteristic of planar sloshing, even close to the moving interface.

The physics-constrained regression of the PTV data was performed with the SPICY framework. We employed Dirichlet no-slip constraints at the contact patches with the walls and Neumann constraints to impose the interface kinematics at the free surface. Moreover, we penalized breaking the divergence-free condition in the global domain. In all tested configurations, the regression error was between 8 and 13%, highlighting the robustness of the RBF framework. The interface and lateral edges were the regions with the largest discrepancies. Nevertheless, our results demonstrate that constraining the regression with the interface dynamics can improve the regression error while providing a fully consistent velocity field with respect to the interface motion. This consistency is particularly useful to validate high-fidelity CFD and any numerical solver for two-phase flows.

Acknowledgment

This work was supported by the European Space Agency (ESA) in the framework of the GSTP-SLOSHII project with reference number 4000129315/19/NL/MG. The authors gratefully acknowledge the financial support of the 'Fonds de la Recherche Scientifique (F.R.S. - FNRS)' for the FRIA grant with reference FC47297 supporting the Ph.D. of Mr. Marques.

References

Abramson, H. N., Dodge, F. T., Bauer, H. F., Brooks, G. W., Chu, W.-H., Dalzell, J. F., … Silverman, S. (1966). *The Dynamic Behavior of Liquids in Moving Containers* (H. N. Abramson, Ed.). NASA.

Ball, M., & Wietschel, M. (2001). The future of hydrogen – opportunities and challenges. *International Journal of Hydrogen Energy*, *34*(2), 615–627.

Barsi, S. (2010). *Ventless pressure control of cryogenic storage tanks* (phdthesis).

Bishop, C. M. (2006). *Pattern recognition and machine learning (information science and statistics)*. Berlin, Heidelberg: Springer-Verlag.

Bäuerlein, B., & Avila, K. (2021). Phase lag predicts nonlinear response maxima in liquid-sloshing experiments. *J. Fluid Mech.*, *925*, A22.

Davin, T., Idlahcen, S., Godard, G., Quevreux, B., Duret, B., & Varea, E. (2023). Optical investigation of a liquid/gas cryogenic flow.

Fonda, E., Sreenivasan, K. R., & Lathrop, D. P. (2012). Liquid nitrogen in fluid dynamics: Visualization and velocimetry using frozen particles. , *83*(8), 085101. Retrieved 2023-12-28, from https://pubs.aip.org/rsi/article/83/8/085101/359073/Liquid-nitrogen-in-fluid-dynamics-Visualization doi:

Fortescue, P., Stark, J., & Swinerd, G. (2003). *Spacecraft systems engineering* (3rd ed.). John Wiley & Sons Ltd.

Heyman, J. (2019). TracTrac: A fast multi-object tracking algorithm for motion estimation. *Computers & Geosciences*, *128*, 11–18.

Ibrahim, R. A. (2005). *Liquid sloshing dynamics: Theory and applications*. Cambridge University Press.

Jeon, G.-M., Park, J.-C., & Choi, S. (2021). Multiphase-thermal simulation on BOG/BOR estimation due to phase change in cryogenic liquid storage tanks. *Applied Thermal Engineering*, *184*, 116264.

Ludwig, C., Dreyer, M., & Hopfinger, E. (2013). Pressure variations in a cryogenic liquid storage tank subjected to periodic excitations. *International Journal of Heat and Mass Transfer*, *66*, 223–234.

Marques, P. A., Simonini, A., Peveroni, L., & Mendez, M. A. (2023, August). Experimental analysis of heat and mass transfer in non-isothermal sloshing using a model-based inverse method. *Applied Thermal Engineering*, *231*, 120871. doi:

Mendez, M., Raiola, M., Masullo, A., Discetti, S., Ianiro, A., Theunissen, R., & Buchlin, J.-M. (2017). Pod-based background removal for particle image velocimetry. *Experimental Thermal and Fluid Science*, *80*, 181-192. Retrieved from https://www.sciencedirect.com/science/article/pii/S0894177716302266 doi:

Miles, J. W. (1984). Resonantly forced surface waves in a circular cylinder. , *149*(-1), 15.

Moran, M. E., McNelis, N. B., Kudlac, M. T., Haberbusch, M. S., & Satornino, G. A. (1994). Experimental results of hydrogen slosh in a 62 cubic foot (1750 liter) tank. In (Vol. NASA Technical Memorandum 106625).

Moya, B., Gonzalez, D., Alfaro, I., Chinesta, F., & Cueto, E. (2019). Learning slosh dynamics by means of data. *Comput Mech*, *64*(2), 511–523.

Otsu, N. (1979). A threshold selection method from gray-level histograms. *IEEE Transactions on Systems, Man, and Cybernetics*, *9*(1), 62-66. doi:

Sculley, D. (2010). Web-scale k-means clustering. In *Proceedings of the 19th international conference on world wide web* (p. 1177–1178). New York, NY, USA: Association for Computing Machinery.

Simonini, A., Peveroni, L., & Vetrano, M. (2019). Simultaneous interface position and bulk velocity measurements in cryogenic sloshing. *Aerospace Science and Technology*, *90*, 452–462.

Simonini, A., Theunissen, R., Masullo, A., & Vetrano, M. (2019). PIV adaptive interrogation and sampling with image projection applied to water sloshing. *Experimental Thermal and Fluid Science*, *102*, 559–574.

Simonini, A., Vetrano, M. R., & Colinet, P. (2016, 07). Cryogenic sloshing investigation by means of non-intrusive measurement techniques..

Sperotto, P., Pieraccini, S., & Mendez, M. A. (2022). A meshless method to compute pressure fields from image velocimetry. *Meas. Sci. Technol.*, *33*(9), 094005.

Sperotto, P., Ratz, M., & Mendez, M. A. (2024). SPICY: a Python toolbox for meshless assimilation from image velocimetry using radial basis functions. *Journal of Open Source Software*, *9*(93). doi:

Verstraete, D., Hendrick, P., Pilidis, P., & Ramsden, K. (2010). Hydrogen fuel tanks for subsonic transport aircraft. *International Journal of Hydrogen Energy*, *35*(20), 11085–11098.